

Phosphor induced significant hole-doping in ferropnictide superconductor $\text{BaFe}_2(\text{As}_{1-x}\text{P}_x)_2$

Z. R. Ye,¹ Y. Zhang,¹ M. Xu,¹ Q. Q. Ge,¹ F. Chen,¹ Juan Jiang,¹ B. P. Xie,¹ J. P. Hu,² and D. L. Feng^{1,*}

¹State Key Laboratory of Surface Physics, Department of Physics, and Advanced Materials Laboratory, Fudan University, Shanghai 200433, People's Republic of China

²Department of Physics, Purdue University, West Lafayette, Indiana 47907, USA

The superconductivity in high temperature superconductors ordinarily arises when doped with hetero-valent ions that introduce charge carriers [1–4]. However, in ferropnictides, “iso-valent” doping, which is generally believed not to introduce charge carriers, can induce superconductivity as well [5–11]. Moreover, unlike other ferropnictides [12, 13], the superconducting gap in $\text{BaFe}_2(\text{As}_{1-x}\text{P}_x)_2$ has been found to contain nodal lines [14–16]. The exact nature of the “iso-valent” doping and nodal gap here are key open issues in building a comprehensive picture of the iron-based high temperature superconductors [17–20]. With angle-resolved photoemission spectroscopy (ARPES), we found that the phosphor substitution in $\text{BaFe}_2(\text{As}_{1-x}\text{P}_x)_2$ induces sizable amount of holes into the hole Fermi surfaces, while the d_{xy} -originated band is relatively intact. This overturns the previous common belief of “iso-valent” doping, explains why the phase diagram of $\text{BaFe}_2(\text{As}_{1-x}\text{P}_x)_2$ is similar to those of the hole-doped compounds, and rules out theories that explain the nodal gap based on vanishing d_{xy} hole pocket.

$\text{BaFe}_2(\text{As}_{1-x}\text{P}_x)_2$ is a rather unique ferropnictide as its superconductivity is introduced by the iso-valent doping of P for As [5, 6]. Unlike the hetero-valent doping that alters the carrier concentration in $\text{Ba}_{1-x}\text{K}_x\text{Fe}_2\text{As}_2$, $\text{BaFe}_{2-x}\text{Co}_x\text{As}_2$, or $\text{LaO}_{1-x}\text{F}_x\text{FeAs}$ [2–4], the iso-valent doping is often considered not to alter the occupation of the Fe 3d bands, as illustrated by the density functional theory calculations of BaFe_2As_2 and BaFe_2P_2 as well [6, 7]. Yet, surprisingly, it has a similar phase diagram just like the hetero-valent doped cases: with P doping, spin density wave (SDW) is suppressed and superconductivity (SC) emerges [6].

Since P anion is smaller than As anion, and thus introduces internal strain or distortion, i.e. chemical pressure, the superconductivity introduced by iso-valent doping is associated with the unprecedented pressure dependence of the superconducting transition temperature (T_c) generally observed in iron-based superconductors [21–24]. In fact, it is the largest among all superconductors in both relative and absolute scales. For example, a T_c dependency of 2-4K/GPa and sometimes even 10K/GPa is observed in $\text{BaFe}_2(\text{As}_{1-x}\text{P}_x)_2$, $\text{LaO}_{1-x}\text{F}_x\text{FeAs}$, etc. [21, 22]; and an increase of T_c from 0 to above 30 K is observed in BaFe_2As_2 and FeSe under pressure [23, 24]. However, these remarkable pressure effects are still far from understood. Theoretically, P doping is predicted to alter the band structure and Fermi surface topology dramatically, considering it changes the electron hopping terms [17, 25]. Particularly, it is predicted that the d_{z^2} -based band would go above the Fermi energy (E_F), while the d_{xy} -based band would move

down below E_F with P doping. Several theories further claim that nodes will appear in the superconducting gap when the d_{xy} hole Fermi pocket disappears [17–19].

Figure 1 examines the dependence of the Fermi surfaces on the P concentration in a series of $\text{BaFe}_2(\text{As}_{1-x}\text{P}_x)_2$, where the photoemission intensity maps near E_F are shown for two k_z 's. The features at the zone center (Γ and Z) are hole pockets, and those at the zone corner (M and A) are electron pockets [26, 28]. As P doping increases, the size of the hole pockets increase significantly, while the electron pockets show negligible doping dependence. This indicates that the P doping could induce extra holes into the system, contradicting to the ordinary picture of iso-valent doping.

To understand such extraordinary P doping effect, more de-

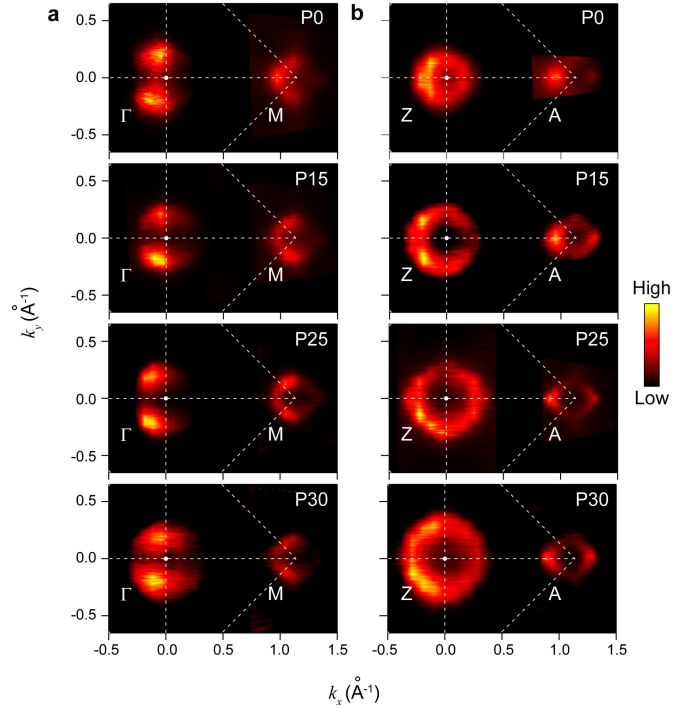


FIG. 1: The doping dependence of the photoemission intensity map in $\text{BaFe}_2(\text{As}_{1-x}\text{P}_x)_2$. **a**, Photoemission intensity maps around Γ and M ($k_z = 0$) in $\text{BaFe}_2(\text{As}_{1-x}\text{P}_x)_2$ for $x = 0, 0.15, 0.25, 0.30$ respectively, named as P0, P15, P25, and P30 hereafter. **b**, is the same as **a**, but taken around Z and A ($k_z = 2\pi/c$). Data around Γ , M, Z, and A were taken at 22 eV, 26 eV, 33 eV, and 17 eV respectively. All data were measured in the paramagnetic state at 150 K, 110 K, 75 K, and 40 K for P0, P15, P25 and P30 respectively to avoid the complications from the electronic structure reconstruction in the SDW and superconducting states [26, 27].

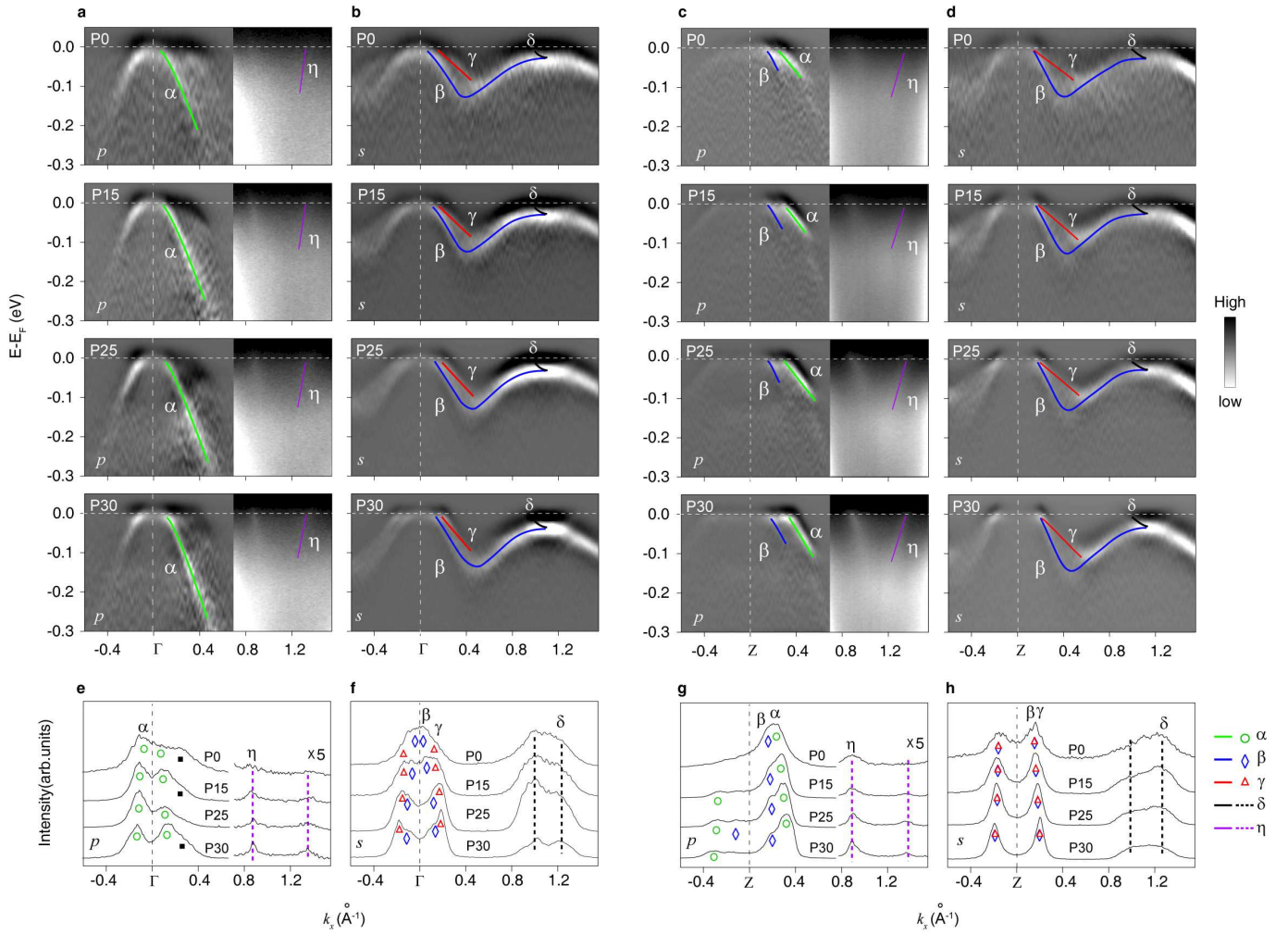


FIG. 2: The doping and polarization dependence of the photoemission data. **a**, Left side: the second derivative with respect to energy of the photoemission intensity taken along Γ -M direction with 118 eV photons for P0 and P15, and 120 eV photons for P25 and P30 in the p polarization; Right side: photoemission intensity highlighting the fast dispersing weak features. **b**, is the same as the left side of **a**, but taken in the s polarization. **e, f**, the corresponding momentum distribution curves (MDC's) near E_F of **a, b**. Note that the right part of **e** is in an expanded intensity scale. The peaks marked by black solid squares in **e** are contributed by the residual spectral weight of the band below E_F with the d_{z^2} orbital (see supplementary information for details). **c, d, g, and h**, are the same as **a, b, e, and f** respectively, but taken along Z-A direction with 100 eV photons. Solid lines are band dispersion, as determined by MDC peaks or the minima of the second derivative of photoemission intensity with respect to energy. Only half of data are overlaid with determined dispersions for a better view of the data.

tailed band structures near E_F are examined with both s and p polarizations of the incoming photons. Since the low-lying electronic structures are mostly made of Fe-3d orbitals with specific even or odd spatial geometry, the photoemission intensity of the even (or odd) component of a band is only detectable with the p or s polarized light [28] (see supplementary information for details). Fig. 2a shows the photoemission data taken around Γ with the p polarization. One could resolve a fast dispersing α band. According to previous studies, the α band corresponds to the even d_{xz} orbital [28]. In the s polarization (Fig. 2b), two bands, β and γ , could be observed. The β band could be assigned to the odd d_{yz} orbital. Although β is almost degenerate with α near E_F , it bends back towards E_F at about 120 meV, instead of further dispersing to higher

binding energies. The γ band is made of the d_{xy} orbital, which shows much weaker intensity than β due to its small matrix element near the Γ point [28]. Around the Z point, however, one could resolve two bands in the p polarization (Fig. 2c). The inner band is contributed by the even component of the β band, since it shows the identical Fermi crossing and band dispersion with the odd component of the β band observed in the s polarization (Fig. 2d). The outer one is the α band, whose Fermi momentum is enlarged significantly from Γ to Z, indicating its remarkably strong k_z dispersion. On the other hand, the Fermi momentum of β moves outward only slightly and becomes degenerate with the γ band around Z.

Two electron-like bands, δ and η , are clearly distinguished in the s and p polarization separately around the zone cor-

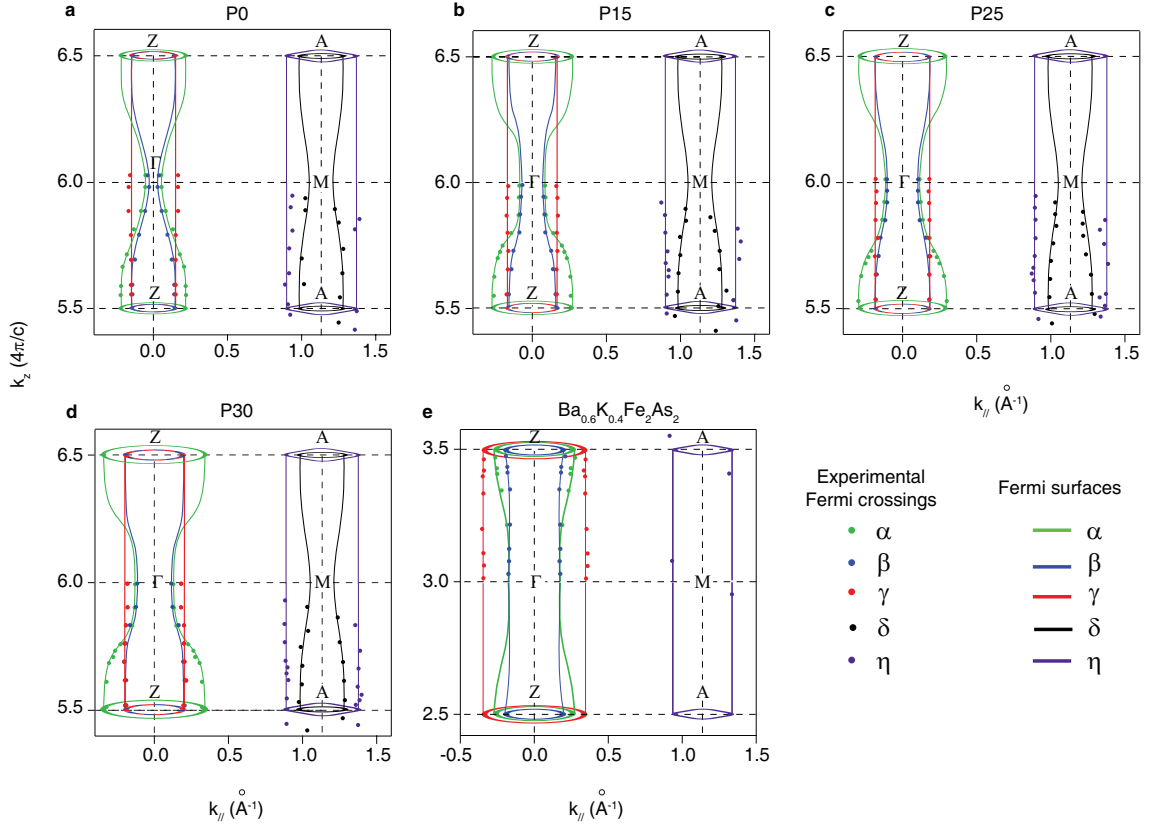


FIG. 3: **The experimental Fermi surface cross-sections in Z- Γ -M-A plane.** **a-d**, Fermi surfaces of P0, P15, P25, and P30 respectively determined based on the experimental Fermi crossings (dots). **e**, Fermi surface of $\text{Ba}_{0.6}\text{K}_{0.4}\text{Fe}_2\text{As}_2$ [27].

ner, consistent with previous studies [28]. Because of the weak intensity, the η band is presented with the photoemission intensity data in Fig. 2a,c, and the Fermi crossings of these two bands together with others could be traced from the corresponding momentum distribution curves (MDC's) near E_F in Fig. 2e-h. It is clear that the Fermi crossings of δ and η show negligible doping dependence, while the Fermi momenta of α , β and γ increase with P doping. Particularly, the α Fermi crossings expand much more exceptionally than the others around Z.

The different behaviors of the band structure between Γ and Z suggest a strong three-dimensional (3D) character of the electronic structure. Through photon energy dependence of the MDC's in both the s and p polarizations (see supplementary information for details), we could determine the Fermi crossings of individual bands. The resulting Fermi surface cross-sections in the k_x - k_z plane are shown in Fig. 3a-d. In all cases, the two electron pockets δ and η at the zone corner show a weak 3D character and negligible doping dependence [7]. The α and β hole pockets increase from Γ to Z, while the γ pockets show almost no k_z dependence, which is consistent with the two-dimensional character of the d_{xy} orbital [28]. With P doping, β and γ Fermi surfaces expand slightly, keeping their shapes basically unchanged. However, the curvature of the α Fermi surface changes significantly, which sug-

gests a strong enhancement of the 3D character of the α band due to P doping. While previous quantum oscillation [7] and ARPES measurements [29] were focused on limited regions of the Brillouin zone, our data over the entire Brillouin zone give direct evidence for the phosphor induced hole doping. Moreover, the three hole pockets observed here complement the previous ARPES study [10], where only two hole pockets were observed due to its particular experimental setup. Furthermore, our results provide compelling evidence that the d_{xy} band still forms the γ Fermi surface near E_F , which is inconsistent with the prediction of band calculations [17–19]. Consequently, our data rule out all the theories that explain nodal gap in $\text{BaFe}_2(\text{As}_{1-x}\text{P}_x)_2$ based on the vanishing d_{xy} Fermi surface [17–19].

The hole doped by phosphor in $\text{BaFe}_2(\text{As}_{1-x}\text{P}_x)_2$ is unexpected. As a comparison, Fig. 3e shows the Fermi surface cross-section of the optimally hole-doped $\text{Ba}_{0.6}\text{K}_{0.4}\text{Fe}_2\text{As}_2$ with a T_c as high as 38 K [27], where the doped potassium is outside the FeAs layer and should not induce much chemical pressure in the FeAs layer. Compared with the undoped case (Fig. 3a), the hole doping in $\text{Ba}_{0.6}\text{K}_{0.4}\text{Fe}_2\text{As}_2$ enlarges the hole pockets, and shrinks the electron pockets as expected in a rigid band picture, where the δ electron pocket even diminishes. On the other hand, the different behaviors of electron and hole pockets in $\text{BaFe}_2(\text{As}_{1-x}\text{P}_x)_2$ manifest its strong

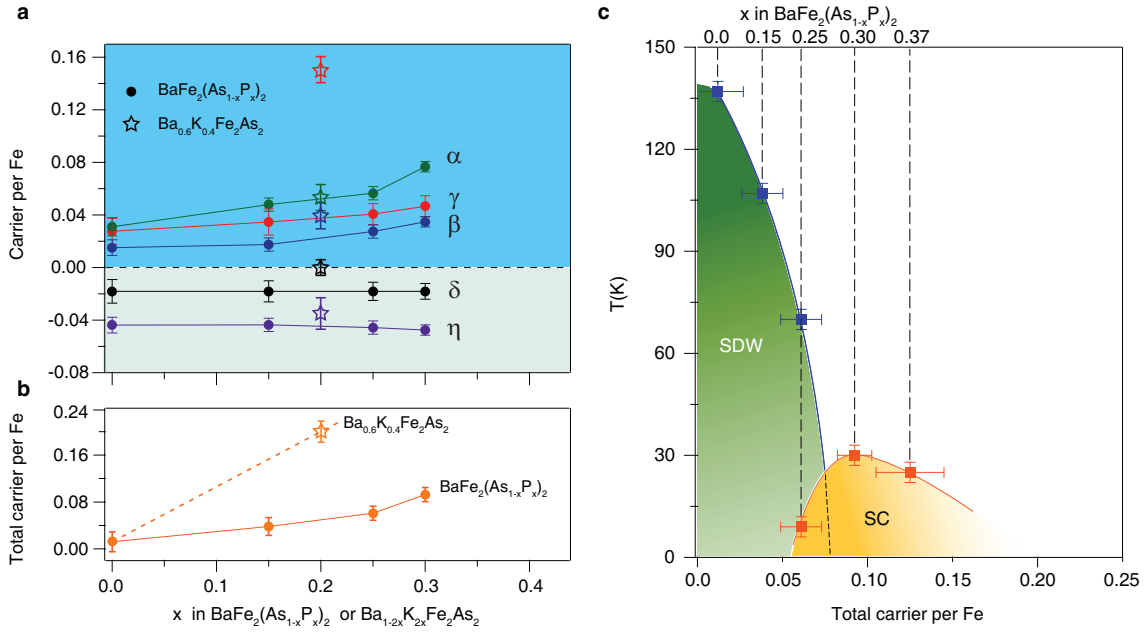


FIG. 4: **Summary of the band-specific carrier density, and phase diagram of BaFe₂(As_{1-x}P_x)₂.** **a**, The carrier density contributed by individual bands, and **b**, the total carrier density in BaFe₂(As_{1-x}P_x)₂ and Ba_{0.6}K_{0.4}Fe₂As₂. **c**, The phase diagram of BaFe₂(As_{1-x}P_x)₂ with respect to the total carrier density. The error bars of carrier density per Fe in **a**, **b**, and **c** are due to the uncertainty in estimating the 3D Fermi surface size. The error bars of the transition temperatures in **c** are obtained from the transport measurement.

non-rigid band nature, which is most likely caused by chemical pressure. More specifically, the γ pocket is much smaller, and the electron pockets (η and δ) are larger in P30 than that in Ba_{0.6}K_{0.4}Fe₂As₂. Another remarkable difference between P30 and Ba_{0.6}K_{0.4}Fe₂As₂ is the α Fermi surface, which exhibits a strong k_z dependence, and becomes the outmost hole pocket around Z in P30. Recent theoretical study has proposed that, with the increasing of the phosphor doping, the weight of d_{z^2} orbital could shift up towards E_F , and strongly mixed into the bands around Z, which could result in the nodal superconducting gap [20]. Since the mixture of d_{z^2} might enhance k_z dependence, our results seem to favor this scenario. Thus, it would be elucidative to study the d_{z^2} component in α , and look for nodes in the superconducting gap on the α Fermi surface around Z. We leave this for further studies.

The charge carrier doping can be estimated from the Fermi surface volume. Fig. 4a summarizes the carriers per Fe contributed by each band. The hole carriers in the α , β , and γ bands increase simultaneously with P doping, with the biggest contribution from the α band. The electron carriers in the δ band remain the same, while those of the η band slightly increase with P doping. Fig. 4b plots the total net carrier per Fe obtained by summing up the contributions from all these five bands. The doping of holes is nearly proportional to the P doping, and one phosphor substitution could induce about 0.3 holes per iron. One possible explanation for such a hole doping comes from the balance between bond length and anion electron negativity. When the bond length is shorter, an anion would take less electrons away from the cation of a covalent

bond. For BaFe₂As₂ and BaFe₂P₂, the Fe-As bond length is 2.3980 Å, and Fe-P bond length is 2.2614 Å respectively [9]. The electronegativity of P (2.19 in Pauling's scale) is larger than that of As (2.18) [30]. The smaller Fe-P bond length and the larger P electronegativity make the charge distribution on the Fe-P covalent bond similar to that of Fe-As. Therefore, holes and electrons in both systems are balanced. However, for light P-doped case, the P substitution could induce local lattice distortion and the Fe-P bond length is larger than that in BaFe₂P₂ (2.2614 Å). As a result, P would take more electrons away from Fe, and the localization of electrons at phosphor sites induces the hole carrier. On the other hand, when the doping is approaching the BaFe₂P₂ end, the hole doping would predictably decrease.

For comparison, the carrier density distribution in Ba_{0.6}K_{0.4}Fe₂As₂ is shown by the pentagles in Fig. 4a,b, where the γ band contributes the most holes into the system rather than the α band in BaFe₂(As_{1-x}P_x)₂. The total carrier density in Ba_{0.6}K_{0.4}Fe₂As₂ is 0.208 ± 0.010 holes per Fe, as expected from the K concentration. That is, the hole doping in Ba_{0.6}K_{0.4}Fe₂As₂ is due to the charge transfer between the FeAs layer and the potassium layer, instead of the localization of electrons in BaFe₂(As_{1-x}P_x)₂. Fig. 4c gives the phase diagram with respect to the total carrier per Fe in BaFe₂(As_{1-x}P_x)₂. It greatly resembles the K-doped case, except that T_c reaches its maximum at 0.09 holes per Fe, instead of 0.2 holes per Fe in Ba_{1-x}K_xFe₂As₂. It suggests that the rise of superconductivity in BaFe₂(As_{1-x}P_x)₂ is not a pure doping effect. Both the doping effect and the chemical-pressure-

induced non-rigid band behavior described above should be considered to explain the phase diagram of “iso-valent” doping in iron-based superconductors.

Recently, it has been demonstrated that the chemical and physical pressure are rather equivalent in $\text{BaFe}_2(\text{As}_{1-x}\text{P}_x)_2$, as the arbitrary combination of both phosphor doping and physical pressure can reproduce the same phase diagram [22]. Based on our results, it is not unnatural to speculate that the drastic physical pressure effect in iron-based superconductors is likely due to the similar electronic structure changes. However, as the physical pressure does not introduce carriers, both electron and hole pockets would vary simultaneously.

To summarize, the iso-valent ionic picture is oversimplified which could not describe the phosphor doping in iron-based superconductors. Our results highlight that both chemical pressure effect on the band structure, and a new route of carrier doping should play important roles in understanding the various distinct properties of $\text{BaFe}_2(\text{As}_{1-x}\text{P}_x)_2$. Particularly, the d_{xy} band does not sink below E_F even at the optimally doped sample, which disproves the theories that tried to explain the nodal gap in $\text{BaFe}_2(\text{As}_{1-x}\text{P}_x)_2$ based on the absence of the d_{xy} Fermi surface. More importantly, the phenomenologies in $\text{BaFe}_2(\text{As}_{1-x}\text{P}_x)_2$ are united with those by carrier doping to some extent; and a possible explanation of the remarkable pressure effects on T_c in iron-based superconductors is given.

* Electronic address: dlfeng@fudan.edu.cn

- [1] Damascelli, A., Hussain, Z. & Shen, Z.-X. Angle-resolved photoemission studies of the cuprate superconductors. *Rev. Mod. Phys.* **75**, 473 (2003).
- [2] Kamihara, Y., Watanabe, T., Hirano, M. & Hosono, H. Iron-based layered superconductor $\text{LaO}_{1-x}\text{F}_x\text{FeAs}$ ($x = 0.05-0.12$) with $T_c = 26$ K. *J. Am. Chem. Soc.* **130**, 3296-3297, (2008).
- [3] Rotter, M., Tegel, M. & F Johrendt, D. Superconductivity at 38 K in the iron arsenide $(\text{Ba}_{1-x}\text{K}_x)\text{Fe}_2\text{As}_2$. *Phys. Rev. Lett.* **101**, 107006 (2008).
- [4] Sefat, A. S. *et al.* Superconductivity at 22 K in Co-doped BaFe_2As_2 crystals. *Phys. Rev. Lett.* **101**, 117004 (2008).
- [5] Shuai, J. *et al.* Superconductivity up to 30 K in the vicinity of the quantum critical point in $\text{BaFe}_2(\text{As}_{1-x}\text{P}_x)_2$. *J. Phys.: Condens. Matter* **21**, 382203 (2009).
- [6] Kasahara, S. *et al.* Evolution from non-Fermi- to Fermi-liquid transport via isovalent doping in $\text{BaFe}_2(\text{As}_{1-x}\text{P}_x)_2$ superconductors. *Phys. Rev. B* **81**, 184519 (2010).
- [7] Shishido, H. *et al.* Evolution of the Fermi Surface of $\text{BaFe}_2(\text{As}_{1-x}\text{P}_x)_2$ on Entering the Superconducting Dome. *Phys. Rev. Lett.* **104**, 057008 (2010).
- [8] Nakai, Y. *et al.* Unconventional superconductivity and antiferromagnetic quantum critical behavior in the isovalent-doped $\text{BaFe}_2(\text{As}_{1-x}\text{P}_x)_2$. *Phys. Rev. Lett.* **105**, 107003 (2010).
- [9] Rotter, M., Hieke, C. & Johrendt, D. Different response of the crystal structure to isoelectronic doping in $\text{BaFe}_2(\text{As}_{1-x}\text{P}_x)_2$ and $\text{Ba}_{1-x}\text{Sr}_x\text{Fe}_2\text{As}_2$. *Phys. Rev. B* **82**, 014513 (2010).
- [10] Yoshida, T. *et al.* Two- and three-dimensional Fermi surfaces and their nesting properties in superconducting $\text{BaFe}_2(\text{As}_{1-x}\text{P}_x)_2$. Preprint at <http://arxiv.org/abs/1008.2080> (2010).
- [11] Wang, C. *et al.* Superconductivity in $\text{LaFeAs}_{1-x}\text{P}_x\text{O}$: effect of chemical pressures and bond covalency. *Europhys. Lett.* **86** 47002 (2009).
- [12] Ding, H. *et al.* Observation of Fermi-surface-dependent nodeless superconducting gaps in $\text{Ba}_{0.6}\text{K}_{0.4}\text{Fe}_2\text{As}_2$. *Europhys. Lett.* **83**, 47001 (2008).
- [13] Terashima, K. *et al.* Fermi surface nesting induced strong pairing in iron-based superconductors. *Proc. Natl. Acad. Sci. U.S.A.* **106**, 7330 (2009).
- [14] Hashimoto, K. *et al.* Line nodes in the energy gap of superconducting $\text{BaFe}_2(\text{As}_{1-x}\text{P}_x)_2$ single crystals as seen via penetration depth and thermal conductivity. *Phys. Rev. B* **81**, 220501 (2010).
- [15] Yamashita, M. *et al.* Nodal gap structure of $\text{BaFe}_2(\text{As}_{1-x}\text{P}_x)_2$ determined by the angle resolved thermal conductivity. Preprint at <http://arxiv.org/abs/1103.0885> (2011).
- [16] Nakai, Y. *et al.* ^{31}P and ^{75}As NMR evidence for a residual density of states at zero energy in superconducting $\text{BaFe}_2(\text{As}_{0.67}\text{P}_{0.33})_2$. *Phys. Rev. B* **81**, 020503 (2010).
- [17] Kuroki, K., Usui, H., Onari, S., Arita, R. & Aoki, H. Pnictogen height as a possible switch between high- T_c nodeless and low- T_c nodal pairings in the iron-based superconductors. *Phys. Rev. B* **79**, 224511 (2009).
- [18] Wang, F., Zhai, H. & Lee, D.-H. Nodes in the gap function of LaFePO , the gap function of the $\text{Fe}(\text{Se},\text{Te})$ systems, and the STM signature of the s_{\pm} pairing. *Phys. Rev. B* **81**, 184512 (2010).
- [19] Thomale, R., Platt, C., Hanke, W. & Bernevig, B. A. Why some Iron-based superconductors are nodal while others are nodeless. *Phys. Rev. Lett.* **106**, 187003 (2011).
- [20] Suzuki, K., Usui, H. & Kuroki, K. Possible three dimensional nodes in the s_{\pm} superconducting gap of $\text{BaFe}_2(\text{As}_{1-x}\text{P}_x)_2$. *J. Phys. Soc. Jpn.* **80** (2011).
- [21] Takahashi, H. *et al.* Superconductivity at 43 K in an iron-based layered compound $\text{LaO}_{1-x}\text{F}_x\text{FeAs}$. *Nature* **453**, 376-378 (2008).
- [22] Klintberg, L. E. *et al.* Chemical pressure and physical pressure in $\text{BaFe}_2(\text{As}_{1-x}\text{P}_x)_2$. *J. Phys. Soc. Jpn.* **79**, 123706 (2010).
- [23] Alireza, P. L. *et al.* Superconductivity up to 29 K in SrFe_2As_2 and BaFe_2As_2 at high pressures. *J. Phys.: Condens. Matter* **21**, 012208 (2009).
- [24] Margadonna, S. *et al.* Pressure evolution of the low-temperature crystal structure and bonding of the superconductor FeSe ($T_c = 37$ K). *Phys. Rev. B* **80**, 064506 (2009).
- [25] Vildosola, V. *et al.* Bandwidth and Fermi surface of iron oxypnictides: Covalency and sensitivity to structural changes. *Phys. Rev. B* **78**, 064518 (2008).
- [26] Yang, L. X. *et al.* Electronic structure and unusual exchange splitting in the spin-density-wave state of the BaFe_2As_2 parent compound of iron-based superconductors. *Phys. Rev. Lett.* **102**, 107002 (2009).
- [27] Zhang, Y. *et al.* Out-of-plane momentum and symmetry-dependent energy gap of the pnictide $\text{Ba}_{0.6}\text{K}_{0.4}\text{Fe}_2\text{As}_2$ superconductor revealed by angle-resolved photoemission spectroscopy. *Phys. Rev. Lett.* **105**, 117003 (2010).
- [28] Zhang, Y. *et al.* Orbital characters of bands in the iron-based superconductor $\text{BaFe}_{1.85}\text{Co}_{0.15}\text{As}_2$. *Phys. Rev. B* **83**, 054510 (2011).
- [29] Shimojima, T. *et al.* Orbital-independent superconducting gaps in iron pnictides. *Science* **332**, 564-567, (2011).
- [30] Pauling, L. The nature of the chemical bond. IV. The energy of single bonds and the relative electronegativity of atoms. *J. Am. Chem. Soc.* **54**, 3570-3582, (1932).

Methods: High quality $\text{BaFe}_2(\text{As}_{1-x}\text{P}_x)_2$ ($x = 0, 0.15, 0.25, 0.30$) single crystals were synthesized without flux. Ba, FeAs and FeP were mixed with the nominal compositions, loaded into an alumina tube, and then sealed into a stainless steel crucible under the Ar atmosphere. The entire assembly was heated to 1673 K and kept for 12 h or longer, and then slowly cooled down to 1173 K at the rate of 4 K/h before shutting off the power. Shiny platelet crystals as large as $2 \times 2 \times 0.05 \text{ mm}^3$ were obtained with residual resistivity ratio of about 10 (see supplementary information for details). The P concentrations, x , were confirmed by an energy dispersive X-ray (EDX) analysis. The ratio of Ba, Fe, and (AsP) is about 1:2.1:1.9 in all samples. The spin density wave (SDW) transition temperatures were 137 K, 100 K, and 65 K in $x = 0$ (P0), $x = 0.15$ (P15), and $x = 0.25$ (P25) samples respectively. Superconductivity were observed in P25 and $x = 0.30$ (P30) samples with $T_c = 9 \text{ K}$ and 30 K respectively. Mixed polarization data were taken at the Beamline 5-4 of Stanford Synchrotron Radi-

ation Lightsource (SSRL). Polarization-dependence data were taken at the SIS beamline of the Swiss Light Source (SLS). All the data were taken with Scienta electron analyzers, the overall energy resolution was 15-20 meV at SLS or 7-10 meV at SSRL depending on the photon energy, and the angular resolution was 0.3 degree. The samples were cleaved *in situ*, and measured under ultra-high-vacuum of $5 \times 10^{-11} \text{ torr}$.

Acknowledgement: This work is supported in part by the National Science Foundation of China, Ministry of Education of China, Science and Technology Committee of Shanghai Municipal, and National Basic Research Program of China (973 Program) under the grant Nos. 2011CB921802 and 2011CBA00102. SSRL is operated by the US DOE, Office of Basic Energy Science, Divisions of Chemical Sciences and Material Sciences. We thank Dr. D.H.Lu for his assistance at SSRL, and Dr. X.Y.Cui and Dr. M.Shi for their assistance at SLS.

Supplementary information for:

Phosphor induced significant hole-doping in ferropnictide superconductor



Z. R. Ye,¹ Y. Zhang,¹ M. Xu,¹ Q. Q. Ge,¹ F. Chen,¹

Juan Jiang,¹ B. P. Xie,¹ J. P. Hu,² and D. L. Feng^{1,*}

*¹State Key Laboratory of Surface Physics, Department of Physics,
and Advanced Materials Laboratory, Fudan University,
Shanghai 200433, People's Republic of China*

²Department of Physics, Purdue University, West Lafayette, Indiana 47907, USA

*Electronic address: dlfeng@fudan.edu.cn

I. SAMPLE DESCRIPTION

High quality $\text{BaFe}_2(\text{As}_{1-x}\text{P}_x)_2$ ($x = 0, 0.15, 0.25, 0.30$) single crystals were synthesized with no flux method. Shining platelet crystals as large as $2 \times 2 \times 0.05 \text{ mm}^3$ were obtained as shown in the inset of Fig. S1a. The resistivity of $\text{BaFe}_2(\text{As}_{0.7}\text{P}_{0.3})_2$ single crystal shows a sharp superconducting transition at 30 K, with the transition width less than 0.5 K (Fig. S1a). The room temperature-to-residual resistivity ratio is ≈ 10.4 , indicating minimal disorder and impurity of the single crystal. The magnetic susceptibility as a function of temperature was measured in a 20 Oe magnetic field (Fig. S1b). A sharp drop in the zero field cooling (ZFC) susceptibility, indicating the magnetic onset of superconductivity, appears at 30K, which is consistent with the zero-resistivity temperature in Fig. S1a. The ZFC and field cooling (FC) curves indicate a bulk superconductivity nature and high quality of the crystals. The phase diagram of $\text{BaFe}_2(\text{As}_{1-x}\text{P}_x)_2$ is shown in Fig. S2

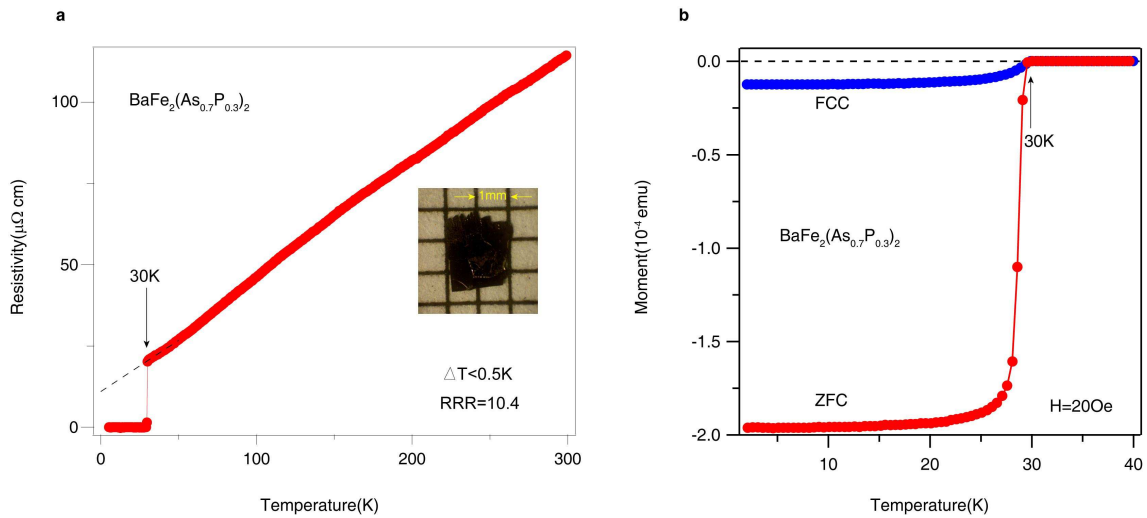


FIG. S1: **Electrical resistivity and magnetic susceptibility of $\text{BaFe}_2(\text{As}_{0.7}\text{P}_{0.3})_2$.** **a**, Temperature dependence of electrical resistivity. The inset is the photography of the $\text{BaFe}_2(\text{As}_{0.7}\text{P}_{0.3})_2$ single crystal. **b**, Temperature dependence of magnetic susceptibility in a 20 Oe magnetic field.

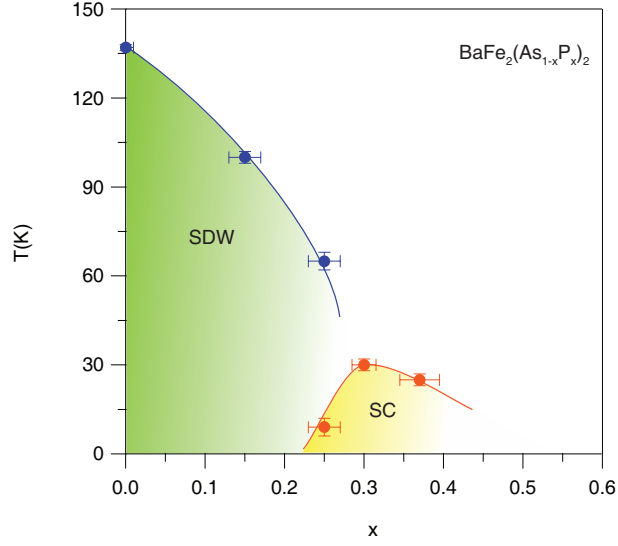


FIG. S2: **Phase diagram of $\text{BaFe}_2(\text{As}_{1-x}\text{P}_x)_2$ with respect to the P doping.** The P concentrations, x , were confirmed by an energy dispersive X-ray (EDX) analysis. With P doping, the spin density wave (SDW) is suppressed and the superconductivity (SC) emerges. The SDW transition temperatures are 137 K, 100 K, and 65 K in $x = 0$ (P0), $x = 0.15$ (P15), and $x = 0.25$ (P25) samples respectively. Superconductivity is observed in P25, $x = 0.30$ (P30), and $x = 0.37$ samples with $T_c = 9$ K, 30 K, and 24.5 K respectively.

II. EXPERIMENTAL SETUP

The polarization-sensitivity of the orbitals in angle-resolved photoemission spectroscopy (ARPES) is a powerful tool to identify the orbital characters of band structure [1, 2]. The matrix element of the photoemission process can be described by

$$|M_{f,i}^{\mathbf{k}}|^2 \propto |\langle \phi_f^{\mathbf{k}} | \hat{\varepsilon} \cdot \mathbf{r} | \phi_i^{\mathbf{k}} \rangle|^2$$

, where $\hat{\varepsilon}$ is the unit vector of the electric field of the light [1]. For high kinetic-energy photoelectrons, the final-state wavefunction $\phi_f^{\mathbf{k}}$ can be approximated by a plane-wave state $e^{i\mathbf{k}\cdot\mathbf{r}}$ with \mathbf{k} in the mirror plane as plotted in Fig. S3c. Consequently, it is always even with respect to the mirror plane. For the p (or s) experimental geometry in Fig. S3c, because $\hat{\varepsilon}$ is parallel (or perpendicular) to the mirror plane, $\hat{\varepsilon} \cdot \mathbf{r}$ is even (or odd). Therefore, to give finite photoemission matrix element, *i.e.* to be observable, the initial state $\phi_i^{\mathbf{k}}$ has to be even (or odd) in the p (or s) geometry.

Considering the spatial symmetry of the $3d$ orbitals (Fig. S3d), when the analyzer slit is along the high symmetry direction of the sample, the photoemission signal of certain orbitals would appear or disappear by specifying the polarization directions as summarized in Table S1. For example, with respect to the mirror plane formed by direction #1 and sample surface normal (or the xz plane), the even orbitals (d_{xz} , d_{z^2} , and $d_{x^2-y^2}$) and the odd orbitals (d_{xy} and d_{yz}) could be only observed in the p and s geometry respectively. Note that, d_{xz} and d_{yz} are not symmetric with respect to the mirror plane defined by direction #2 and surface normal, thus could be observed in both the p and s geometries.

TABLE S1: **The possibility to detect $3d$ orbitals along two high symmetry directions in the p and s geometry by polarization-dependent APRES.**

High-symmetry direction	Experimental geometry	3d orbitals				
		d_{xz}	$d_{x^2-y^2}$	d_{z^2}	d_{yz}	d_{xy}
#1 $\Gamma(\text{Z})$ -M(A)	p	√	√	√		
	s				√	√
#2 $\Gamma(\text{Z})$ -X(R)	p	√		√	√	√
	s	√	√		√	

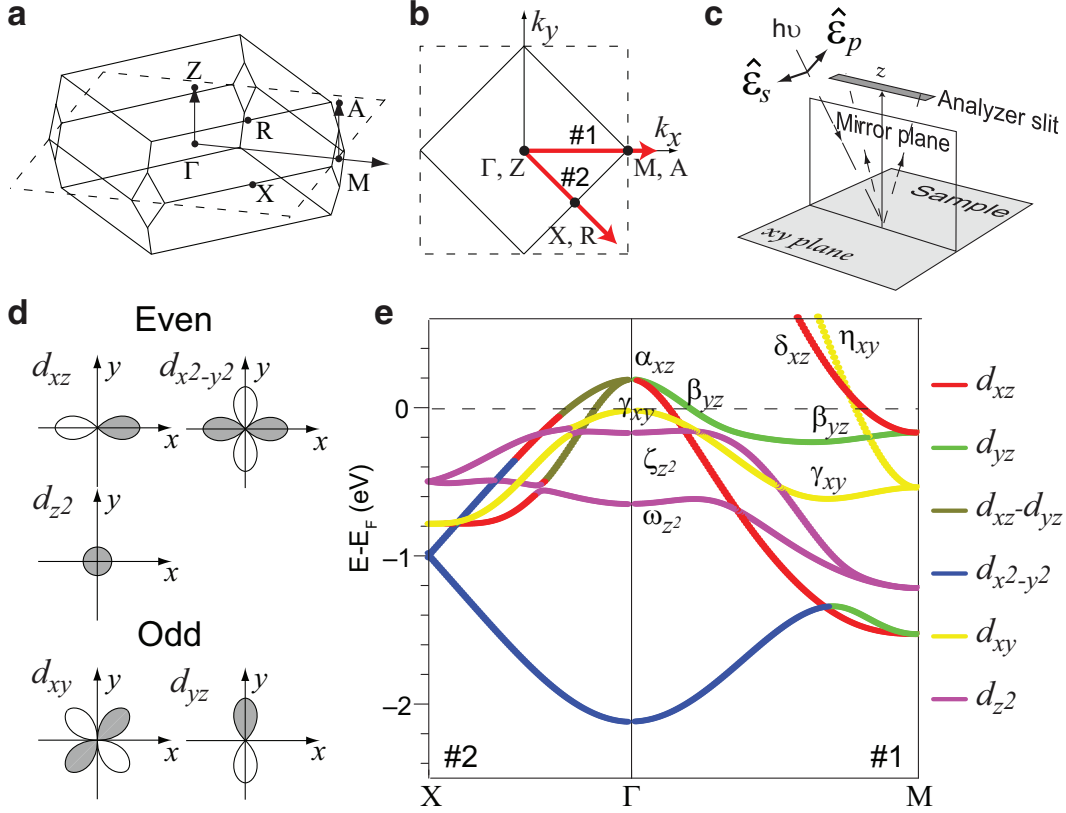


FIG. S3: **The experimental setup and definitions.** **a**, The illustration of the Brillouin zone of BaFe₂As₂. **b**, Two-dimensional plot of the simplified Brillouin zone (solid line) and the unfolded Brillouin zone (dashed line). **c**, Experimental setup for polarization-dependent ARPES. For the p (or s) experimental geometry, the electric field direction of the incident photons $\hat{\epsilon}_p$ (or $\hat{\epsilon}_s$) is parallel (or perpendicular) to the mirror plane defined by the analyzer slit and the sample surface normal. **d**, Illustration of the spatial symmetry of the 3d orbitals with respect to the mirror plane formed by surface normal and cut #1 in panel b, *i.e.* the xz plane. **e**, A typical orbital assignment of bands of iron pnictide as calculated in Ref. [3].

III. d_{z^2} ORBITAL

Besides of the fast dispersing α band, another peak-like feature could be observed in the momentum distribution curves (MDC's) in the inset of Fig. S4a, as pointed out by an arrow. Note that, the d_{z^2} orbital contributes to one band (ζ), which is 200 meV below E_F (Fig. S3e) [2]. This band disperses towards the α band, resulting in an enhancement of the spectral weight at the band crossings (Figs. S4a, b). The resulted intense spectral weight would extend some residual weight towards E_F (Fig. S4c) due to its broad peak width, which forms the non-dispersing peaks in MDC's as marked by the solid squares in Fig. S4d. Therefore, the peak-like feature (ζ) observed in the p polarization at E_F is not the Fermi crossing of band, but the residual spectral weight of ζ well below E_F .

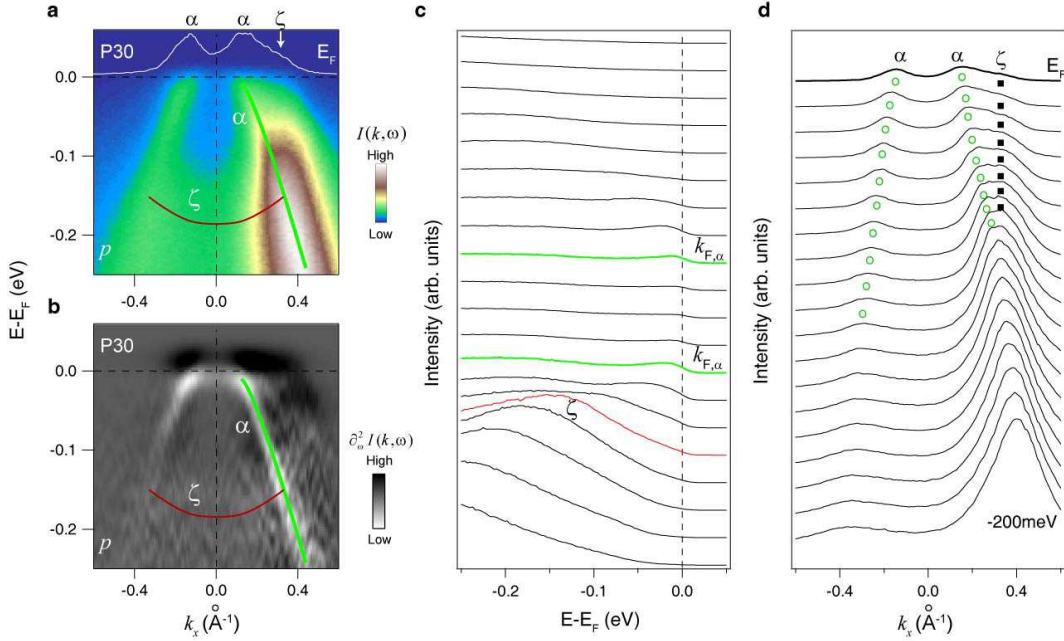


FIG. S4: **The photoemission data of P30 near E_F taken in the p polarization.** **a, b**, The photoemission intensity ($I(k, \omega)$) and its second derivative with respect to energy ($\partial^2 I(k, \omega)/\partial \omega^2$) taken with 120 eV photons around Γ in the p polarization, respectively. Solid lines are band dispersion, as determined by momentum distribution curve (MDC) peaks or the minima of the second derivative of photoemission intensity with respect to energy. The inset in **a** is the MDC at E_F . **c, d**, The energy distribution curves (EDC's) and MDC's of the data in **a**, respectively.

IV. PHOTON ENERGY DEPENDENCE

By changing the photon energy in ARPES experiment, one can probe the different k_z values, according to the following formula [4]:

$$k_{\parallel} = \frac{\sqrt{2m}}{\hbar}[(h\nu - \Phi)]^{1/2} \sin \theta$$
$$k_z = \frac{\sqrt{2m}}{\hbar}[(h\nu - \Phi)\cos^2\theta + V_0]^{1/2}$$

where m and \hbar are the electron mass and Plancks constant, ν is the photon energy, Φ is the work function, and V_0 is the inner potential of the sample, which could be determined experimentally. Through matching the periodicity of the photon energy dependence to the high symmetry points of the Brillouin zone along k_z direction, the inner potential (V_0) is set to 16 eV for calculating the k_z 's in our experiment.

Fig. S5 shows the photon energy dependence of the MDC's near E_F . The Fermi crossings of different bands could be traced separately in the s and p polarization. The peak positions of the MDC's are marked by combining the highest intensity and the center of mass, which is a reliable way and is practiced commonly in ARPES community. Note that, while the α band move outwards from Γ to Z, the even d_{xz} orbital in the α band could mix into the β band. As shown in Figs. S5e-h, when the k_z moves away from Γ , two peaks could be identified corresponding to the α and β bands in the p polarization. The intensity transfer between the MDC peaks of α and β observed in the p polarization is due to the k_z dependence of the even orbital mixing between the α and β band.

-
- [1] Damascelli, A., Hussain, Z. & Shen, Z.-X. Angle-resolved photoemission studies of the cuprate superconductors. *Rev. Mod. Phys.* **75**, 473 (2003).
- [2] Zhang, Y. *et al.* Orbital characters of bands in the iron-based superconductor BaFe_{1.85}Co_{0.15}As₂. *Phys. Rev. B* **83**, 054510 (2011).
- [3] Graser, S., Maier, T. A., Hirschfeld, P. J. & Scalapino, D. J. Near-degeneracy of several pairing channels in multiorbital models for the Fe-pnictides. *New J. Phys.* **11**, 025016 (2009).
- [4] Hufner, S., Photoelectron Spectrsoscopy. *Springer* (1995) .

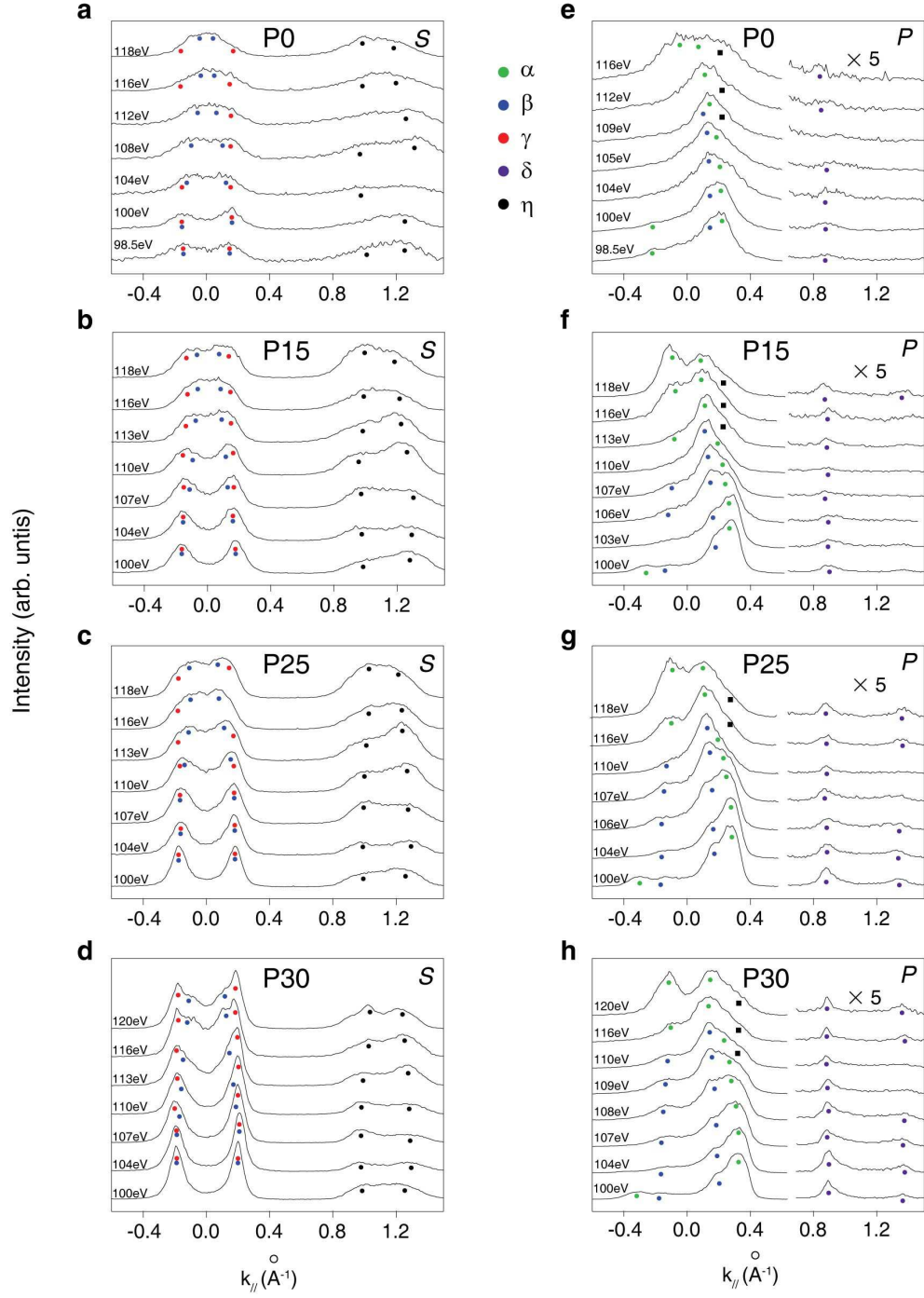


FIG. S5: The photon energy and doping dependence of the MDC's near E_F in the s and p polarizations. **a-d**, The photon energy dependence of the MDC's near E_F taken in the s polarization in P0, P15, P25, and P30 samples, respectively. **e-h**, are the same as **a-d**, but taken in the p polarization. Note that the right parts of **e-h** are in an expanded intensity scale. The peaks marked by black solid squares are contributed by the residual spectral weight of the band below E_F with the d_{-2} orbital